JACS
JOURNAL OF THE AMERICAN CHEMICAL SOCIETY
Article
pubs.acs.org/JACS

Y-doped Li_8ZrO_6: A Li-Ion Battery Cathode Material with High Capacity

Shuping Huang,[†,§] Benjamin E. Wilson,[‡,§] Bo Wang,[†] Yuan Fang,[‡] Keegan Buffington,[‡] Andreas Stein,*[,‡] and Donald G. Truhlar*[,†]

[†]Department of Chemistry, Chemical Theory Center, and Supercomputing Institute and [‡]Department of Chemistry, University of Minnesota, 207 Pleasant Street S.E., Minneapolis, Minnesota 55455-0431, United States

Supporting Information

ABSTRACT: We study—experimentally and theoretically—the energetics, structural changes, and charge flows during the charging and discharging processes for a new high-capacity cathode material, Li_8ZrO_6 (LZO), which we study both pure and yttrium-doped. We quantum mechanically calculated the stable delithiated configurations, the delithiation energy, the charge flow during delithiation, and the stability of the delithiated materials. We find that Li atoms are easier to extract from tetrahedral sites than octahedral ones. We calculate a large average voltage of 4.04 eV vs Li/Li^+ for delithiation of the first Li atom in a primitive cell, which is confirmed by galvanostatic charge/discharge cycling data. Energy calculations indicate that topotactic delithiation is kinetically favored over decomposition into Li, ZrO_2, and O_2 during the charging process, although the thermodynamic energy of the topotactic reaction is less favorable. When one or two lithium atoms are extracted from a primitive cell of LZO, its volume and structure change little, whereas extraction of the third lithium greatly distorts the layered structure. The Li_6ZrO_6 and Li_5ZrO_6 delithiation products can be thermodynamically metastable to release of O_2. Experimentally, materials with sufficiently small particle size for efficient delithiation and relithiation were achieved within an yttrium-doped LZO/carbon composite cathode that exhibited an initial discharge capacity of at least 200 mAh/g over the first 10 cycles, with 142 mAh/g maintained after 60 cycles. Computations predict that during the charging process, the oxygen ion near the Li vacancy is oxidized for both pure LZO and yttrium-doped LZO, which leads to a small-polaron hole.

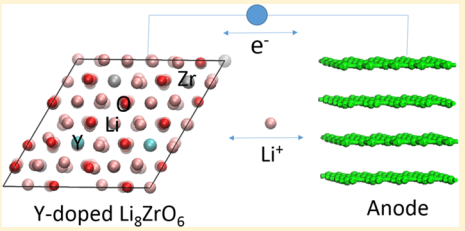

1. INTRODUCTION

Rechargeable Li-ion (Li-ion) batteries have proved useful for energy storage in small devices and transportation.[1−5] Compared with most other kinds of batteries, Li-ion batteries have a higher output voltage and higher energy storage density, and they are more environmentally friendly. They have been widely used in portable electronic devices and are starting to be used in electric vehicles. A Li-ion battery has three major components, the anode, the cathode, and the electrolyte that transfers lithium ions between the two electrodes during the charging and discharging processes. The electrochemical reactions in the discharging step can be written as

$$\text{anode:}\quad \mathrm{Li} \rightarrow \mathrm{Li^+} + \mathrm{e^-} \tag{1}$$

$$\text{cathode:}\quad \mathrm{Li}_x\mathrm{M} + \mathrm{Li^+} + \mathrm{e^-} \rightarrow \mathrm{Li}_{x+1}\mathrm{M} \tag{2}$$

$$\text{total reaction:}\quad \mathrm{Li}_x\mathrm{M} + \mathrm{Li} \rightarrow \mathrm{Li}_{x+1}\mathrm{M} \tag{3}$$

where "M" denotes a cathode host material in which the Li^+ can be reversibly inserted and extracted. We simply wrote "Li" for the anode material, although in practice the most widely used anodes are either lithium metal in half-cell tests or lithium metal intercalated into graphite in practical lithium ion batteries.[3]

The selection of the cathode materials affects the output potential and storage capacity of the battery as well as the stability and the safety of the battery. Various kinds of cathode materials have been investigated and used in applications,[2,5] including layered structures, such as $LiCoO_2$ and $LiNiO_2$, spinel structures, such as $LiMn_2O_4$, and olivine structures, such as $LiFePO_4$. Considerable research has been devoted to exploring new materials and structures to improve battery performance, including the Li^+ diffusion rate, the electric potential and storage capacity, and how the number of cycles affects battery life. One example of progress is the improvement of the Li^+ diffusion rate in $LiNi_{0.5}Mn_{1.5}O_4$ through the control of disorder.[6] More sophisticated structures, such as nanostructured and porous electrodes,[7−9] are also promising for improving the performance of batteries.

Computational simulations provide a supplementary tool to understand Li-ion battery properties at the atomic level, and they can be used to design and to optimize new materials for lithium batteries. Both classical calculations[10−12] and quantum mechanical calculations[13−19] have been carried out on Li-ion batteries. In the latter, approximate solutions are obtained for the Schrödinger equation or the Kohn−Sham equations describing the electronic structure of the materials. Intercalation potentials, structural changes during the charging and discharging processes, diffusion rates, and other properties can be derived from such studies.[13] Many promising materials,

Received: May 5, 2015
Published: August 11, 2015

DOI: 10.1021/jacs.5b04690
J. Am. Chem. Soc. 2015, 137, 10992−11003

such as Li_xCoO_2,[20−23] $Li_2Ti_2O_4$,[24] $LiMn_2O_4$,[25] $LiTiS_2$,[26] $LiFePO_4$,[27] $LiMSiO_4$ (M = Fe, Mn, Co, Ni),[28−32] have been systematically studied.

In the present article, we carry out density functional electronic structure calculations by Kohn−Sham theory (KST)[33] for a new cathode material, namely octalithium zirconate, Li_8ZrO_6 (LZO), to evaluate its feasibility for use in lithium ion batteries. LZO has a layered structure suitable for intercalation and deintercalation of lithium and has a high theoretical specific capacity because there are multiple lithiums in each formula unit. Given its high lithium content, it has been studied as a potential tritium breeding material in fusion reactors.[34] It has also been modeled as a CO_2 absorbent.[35] Calculations indicate that it may have a redox potential vs Li/Li^+ that is >3.5 eV.[35,36] However, it has not been systematically studied for Li-ion battery use, except as a solid electrolyte coating.[37] Compared with conventional cathode materials, LZO has a large band gap and low conductivity, lacks a transition metal with multiple oxidation states, and has a slow ion diffusion rate. However, the low conductivity may be overcome by synthesizing smaller particles since small dimensions increase the surface/volume ratio and shorten electron conduction and Li diffusion lengths. This has been demonstrated for other cathode materials with limited conductivity, such as $LiFePO_4$, which is now a commercial cathode material for Li-ion batteries.[7] The production of LZO with small enough grains sizes, in the 30−50 nm range, for efficient delithiation and relithiation was achieved in the present work by the development of a method for producing yttrium-doped LZO/carbon composites, in which nanoparticles of doped LZO are in intimate contact with a conductive carbon phase.

The present study concentrates on structure and energetics of LZO and yttrium-doped LZO with experimental support for some of the theoretical predictions. This includes voltage and volume change as the intercalated Li is removed, charge flow during reactions, and the stability of the delithiated compounds. The study also presents galvanostatic data that demonstrate the prospect of yttrium-doped LZO as a high capacity cathode material for Li-ion batteries.

2. METHODS

2.1. Preparation of LZO. The synthesis of LZO was accomplished by the thermal decomposition of nitrate precursors, following a procedure slightly modified from a previous published synthesis;[38] this yields LZO as a microcrystalline powder. Zirconium oxynitrate (4.2 mmol) and lithium nitrate (42 mmol) were ball-milled in a zirconia ball and cup set for 5 min and then calcined in a covered alumina crucible at 2 °C/min to 600 °C, followed by a 3 h isothermal step, further heating at 2 °C/min to 800 °C, and an additional 2 h isothermal step at 800 °C. (Molar calculations were performed using the anhydrous basis for the lithium and zirconium nitrate precursors, and 243.22 g/mol was used for zirconium acetate hydroxide $[Zr(C_2H_3O_2)_x(OH)_y$, $x = y = 2]$, below.) The as-made product was ground to a fine powder using an agate mortar and pestle prior to further analysis.

2.2. Preparation of LZO/C Composites. To intimately mix the active material with a conductive phase, a more complex composite synthesis was used. First, zirconium acetate hydroxide (4.1 mmol), lithium acetate dihydrate (41 mmol), and Super P carbon (0.25 g) were ball milled for 5 min, followed by the addition of 0.25 g of stock PF solution. The composite was mixed well prior to curing the resol at 120 °C for 24 h. The dry powder was briefly ground using an agate mortar and pestle prior to pyrolysis under 0.5 L/min N_2 following the same thermal parameters as for the bulk LZO. The final product was found to be 22.1 wt % carbon, as determined by combustion-based analysis, performed by Atlantic Microlabs, Norcross, GA.

Additionally, Y-doped samples were prepared starting from yttria-doped ZrO_2 nanoparticles on the surface of conductive carbon, made through a synthesis adapted from Jiang et al.[39] In this synthesis, carbon black mitigates agglomeration of ZrO_2 nanoparticles, and the yttrium is believed to reduce grain growth by lowering the surface energy of ZrO_2 grains or decreasing the concentration of mobile species on the grain surface.[40] Briefly, zirconyl nitrate (3.24 mmol) and yttrium nitrate (0.207 mmol) were dissolved in a solution of nitric acid (0.2 g) and deionized water (15.8 g). The solution was added in four parts to Super P carbon (1.66 g), with each part thoroughly mixed with a mortar and pestle, then dried before adding the next portion. After the final addition, the mixture was dried at 110 °C for 1 h, heated to 400 °C under static air at 2 °C/min, then cooled naturally to ambient temperature. The nanoparticles were converted to LZO by ball milling the ZrO_2/C with lithium benzoate at 10:1 Li:Zr (based on residual mass from thermogravimetric analysis) for 5 min, then carbonizing the composite at maximum temperature (700, 750, 800, 850, or 900 °C) with a 1 °C/min ramp to 600 °C, followed by a 2 h hold, then 2 °C/min to the target temperature, followed by another 2 h hold, all under 0.5 L/min N_2 flow. The product was allowed to completely cool to room temperature before being removed from the inert atmosphere because partial self-combustion can occur at temperatures exceeding ∼35 °C in the presence of air. The final products contained between 55−60 wt % carbon, as determined by combustion-based analysis, performed by Atlantic Microlabs, Norcross, GA, and are referred to as Y−Li_8ZrO_6/C or Y-LZO-*T*, where the value of *T* refers to the maximum heating temperature in °C.

These composite materials were used for ex situ X-ray diffraction (XRD), X-ray photoelectron spectroscopy (XPS), and electrochemical measurements.

2.3. Battery Assembly. Electrodes were made from the LZO/C composites by first grinding Super P carbon (26.0 mg) and the composite (154 mg) using an agate mortar and pestle for 5 min to create a uniform mixture. We added 200 mg of a 10 wt % solution of polyvinylidene diflouride (PVDF), in *N*-methylpyrrolidone, an (NMP), and additional NMP (∼1 mL), and we mixed the solution for 5 min to create a viscous slurry with a final dry composition of 60:30:10 Li_8ZrO_6:C:PVDF by weight. Because the yttrium-doped sample contained a significant amount of carbon in the composite, a slurry of this material was prepared without additional carbon, using a 90:10 weight ratio of composite:PVDF. The slurry was then cast onto carbon-coated aluminum foil using a doctor blade and dried at ambient temperature in a dry room maintained below 80 ppm of H_2O or 1% relative humidity during active use. The dried film was pressed using a roller press to approximately half of its original thickness (final thickness ∼250 μm), and 0.5 in. diameter disks were punched out. Active material loading was between 2 and 2.5 mg/cm^2. The electrodes were assembled into CR2032 coin cells in a half-cell configuration with metallic lithium as the counter electrode. A Celgard 3501 polypropylene membrane was used as the separator and 1 M $LiPF_6$-ethylene carbonate, dimethyl carbonate, and diethyl carbonate (EC-DMC-DEC) as the electrolyte. A wave spring was used behind the current collectors to maintain pressure and electrical contact within the cell. All assembly was done in a He-filled glovebox.

2.4. Electrochemical Measurements. Following the usual convention for reporting battery charging and discharging rates, we define 1 C as a rate of one Faraday constant per mol of Li_8ZrO_6 per hour; this yields 1 C equal to 110.5 mA/g. All galvanostatic cycling was performed between 1.3 and 4.5 V vs Li/Li^+.

2.5. Product Characterization. A series of coin cells was made from a single film and driven at a constant current of C/5 to different charged or discharged states, followed by cell disassembly and ex situ powder XRD (PXRD) analysis.

XPS data were obtained, and XPS peak positions were calibrated against the $C_{1s(sp^3)}$ peak of (adventitious) carbon, set at 284.6 eV.

UV−vis spectra were obtained, and a Kubelka−Munk transformation[41] was performed on the UV−vis spectrum of LZO using the following equation:

DOI: 10.1021/jacs.5b04690
J. Am. Chem. Soc. 2015, 137, 10992−11003

$$F(R) = \frac{(1 - R)^2}{2R} \quad (4)$$

where $F(R)$ is the Kubelka–Munk remission function, and R is reflectance.[42] The UV–vis spectrum of semiconductors near the absorption edge is described by the following equation:

$$F(R)h\nu = B(h\nu - E_g)^n \quad (5)$$

in which $h\nu$ is the energy of a photon, B is a coefficient, and E_g is the band gap. Our computational results show that LZO has an indirect band gap, so we set n equal to 2, which is the appropriate value for allowed transitions with an indirect band gap. Therefore, the optical band gap was determined by plotting $(F(R)h\nu)^{1/2}$ against $h\nu$ (which is known as a Tauc plot),[43] and E_g was obtained by extrapolating the linear part to $F(R) = 0$.

2.6. Density Functional Calculations. The structure of Li_8ZrO_6 has a space group of $R\bar{3}$, with a and b parameters of 5.483 Å and c equal to 15.45 Å in the conventional unit cell.[44] The oxygen atoms are stacked in an *ABAB* hexagonally close-packed anion sublattice. The Zr ions fill octahedral sites between the close-packed O planes, and the Li ions fill both octahedral sites (O_h) and tetrahedral sites (T). The crystal can be viewed as an array of Li_2ZrO_6 slabs separated by two layers of Li ions with three Li in each layer. The conventional unit cell and primitive cell of Li_8ZrO_6 are shown in Figure 1.

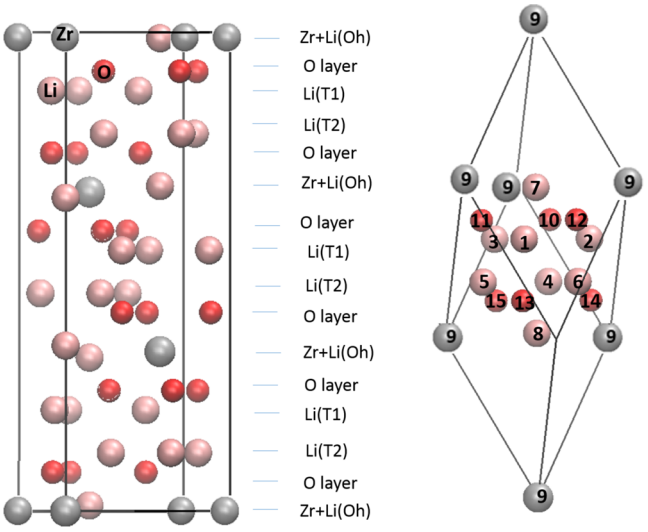

Figure 1. (a) Conventional unit cell of LZO. The oxygen ions form close-packed planes, the zirconium ions occupy octahedral voids, and the lithium ions occupy tetrahedral voids (labeled as T1 and T2) and octahedral voids (labeled as Oh). (b) Primitive cell of LZO. Li1–Li6 are in tetrahedral voids and Li7–Li8 are in octahedral voids.

Quantum mechanical calculations were carried out employing several exchange–correlation density functionals. In most cases we used the HSE06,[45] M06-L,[46] N12,[47] and PBE[48] functionals, but in a few cases we examine the sensitivity to the choice of functional by also considering results obtained with one or more of these other functionals: N12-SX,[49] PBE0,[50] and PW91.[51] The M06-L, N12, PBE, and PW91 functionals are local; the HSE06 and N12-SX functionals have screened nonlocal Hartree–Fock exchange (decreasing from 25% at small interelectronic separation to zero at large interelectronic separation), and PBE0 has 25% nonlocal Hartree–Fock exchange at all interelectronic separations. The functionals with Hartree–Fock exchange are expected to give more accurate band structures and polaron descriptions, but Hartree–Fock exchange also brings in static correlation error.

We also used the PBE+U method; this method has been extensively used in the study of transition-metal oxides where the Coulomb and exchange interactions of the d orbitals of the transition metal are corrected by the empirical GGA+U[52−54] method, and the other electrons are treated by the uncorrected PBE exchange–correlation functional. Since the oxygen 2p orbitals contribute to the top of the valence bands of LZO, we applied the U correction to these orbitals in studying the delithiation process. Previous studies of other systems with O 2p holes determined that a U value in the range of 5–7 eV can best reproduce experimental findings.[55−57] Therefore, the central value U = 6.0 eV is applied to oxygen in our PBE+U calculation.

All calculations included spin polarization. Both the coordinates of the atoms and the lattice constants were optimized.

The averaged Li cell potentials vs Li/Li^+ were calculated as

$$V = -\frac{1}{F}\frac{E(Li_xM) - E(Li_{x-\Delta x}M) - \Delta xE(Li)}{\Delta x} \quad (6)$$

where E is the total energy, and F is the Faraday constant. These are average potentials over the range of x from $x - \Delta x$ to x. For the undoped material, "M" denotes "ZrO_6".

The substitution of Y^{3+} for Zr^{4+} results in the creation of oxygen vacancies in the Y-doped ZrO_2 precursor, and we expect the same for the Y-doped LZO. Hence the Y-doping was simulated using a supercell ($Li_{96}Zr_{12}O_{72}$), which is a 2 × 2 × 1 repetition of the conventional cell. Two Zr in the supercell were replaced by two Y, and one O was removed for charge compensation.

3. RESULTS AND DISCUSSION

3.1. Structures of LZO and Y-LZO/C. We used six density functional methods to optimize the structure of LZO, and the optimized unit cell parameters are shown in Table 1. It is found that M06-L and PBE+U give the most accurate lattice parameters, and HSE06 and PBE0[58] also give accurate geometries compared with experiment. The XRD pattern was simulated using the M06-L optimized structure and compared with both the experimental pattern from microcrystalline LZO and the pattern of the Rietveld-refined structure (Figure 2a and Tables S1 and S2). The computational pattern matches very well with the observed and refined patterns in both peak intensities and positions. Furthermore, the atomic positions obtained by Rietveld refinement of the experimental pattern and M06-L and HSE06 computational methods are nearly identical, further verifying the functionals. The lattice parameters of the unit cell in space group 148 ($R\bar{3}$) are also very similar for the refined structure and both of these functionals (Table S3). Overall, the close match between the computed and experimental parameters directly validates the ability of the M06-L and HSE06 functionals to accurately model the LZO crystal structure. In addition, this work confirms the structure of LZO that was previously only established by analogy to the powder pattern of Li_8SnO_6.[59,60]

Table 1. Lattice Parameters of Li_8ZrO_6 Determined from Rietveld Refinement and Optimized by Various Density Functionals

	$a = b$ (Å)	c (Å)	volume (Å^3)
literature[a]	5.48	15.45	402
Rietveld refinement (this study)	5.49	15.47	404
PBE	5.51	15.58	410
N12	5.43	15.38	393
M06-L	5.46	15.46	399
HSE06	5.46	15.39	397
PBE0	5.45	15.43	398
PBE+U	5.47	15.46	400

[a]Ref 44.

DOI: 10.1021/jacs.5b04690
J. Am. Chem. Soc. 2015, 137, 10992–11003

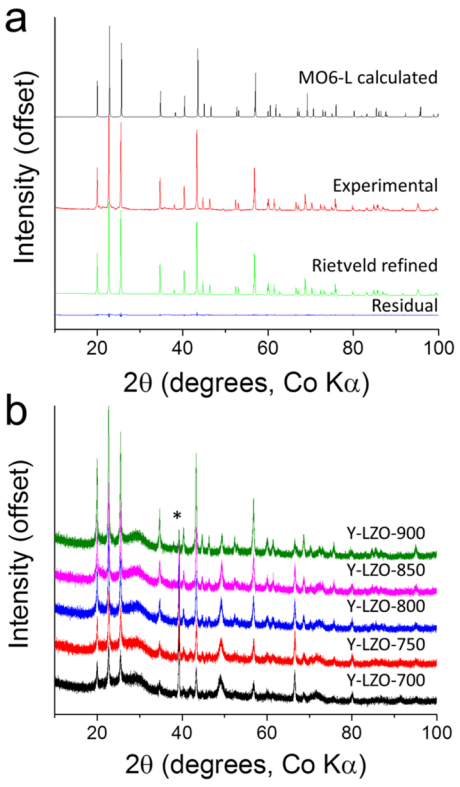

Figure 2. (a) Comparison of the calculated XRD pattern of LZO as determined from the M06-L functional to the experimental pattern and the pattern of the Rietveld-refined structure. The residual trace confirms the close match between the experimental and Rietveld patterns. (b) Experimental XRD patterns for the Y–Li_8ZrO_6/C composite material used for galvanostatic charging/discharging. The asterisk marks a reflection corresponding to a minor Li_2O secondary phase.

The powder patterns of the Y-LZO/C composites also match the Rietveld refined pattern (Figure 2b), indicating that the yttrium doping does not significantly alter the crystal structure. The formation energy of oxygen vacancies is highly reduced in Y-LZO compared with LZO. The stability of two Y atoms at different layers and different distances was compared. It was found that the two Y atoms prefer to be in the same layer and to be close to each other (d_{Y-Y} = 5.50 Å). The different positions of the O vacancy were also considered. The O vacancy prefers Y coordination, which is different from Y-doped ZrO_2, in which O vacancy prefers Zr coordination.[61] The calculated lattice constants for Y-LZO are very slightly increased compared with the undoped material, and this small shift is also observed in the experimental patterns (Table S4).

3.2. Electronic Structure. To determine band structure, different functionals were first tested with ZrO_2, and their performance was compared with experimental results[62] (Table S5). It was found that in the case of ZrO_2, the calculated lattice constants and gap by HSE06 are in good agreement with experimental results. M06-L underestimates the band gap. The gap with N12-SX is within the range of experimental ones. A band gap calculation was then performed on Li_8ZrO_6. The band gaps from various functionals are shown in Table 2. The band structure of Li_8ZrO_6 shown in Figure 3a was calculated with a local functional, M06-L, and it has an indirect band gap of 5.3 eV. It is well-known that local functionals underestimate semiconductor band gaps significantly,[63−65] but their predictions are still of interest because they can be used conveniently for exploratory work on trends, which they predict more accurately than they predict absolute values. Among the functionals used, the HSE06 and N12-SX hybrid functionals, which include Hartree−Fock exchange, have the smallest error (0.3 eV) in predicting the gaps of 31 semiconductors.[64,65] The calculated LZO gap by HSE06 and N12-SX is 6.8 and 6.5 eV, respectively.

Our density functional calculations indicate an indirect band gap (Figure 3a). Experimentally, the band gap of LZO was determined from the diffuse reflectance UV−vis spectrum (shown in Figure 3b) by applying a Kubelka−Munk transformation and Tauc plot, as discussed in the Methods section. This indicated a band gap of 5.75 eV. The HSE06 and N12-SX functionals overestimate the gap by about 0.7 and 1.0 eV, respectively. The large band gap signifies that LZO has poor electronic conductivity, which needs to be compensated by forming a nanocomposite with a conductive phase to allow the use of LZO as active material in an electrode, preferably with very small particle sizes.

We also calculated the density of states (DOS), and we calculated the partial density of states (PDOS) for each atomic number by integrating the electron density around atoms having a given atomic number; for these integrations we used sphere radii adjusted to match the CM5[66] partial atomic charges to within 0.01 (Figure 4). We found that changing the integrating radii for the atoms can significantly change the PDOS figure, a circumstance that is not usually noted in the literature. A detailed comparison between different radii is shown in Table S6 and Figures S1 and S2. The bottom of the conduction bands is dominated by the density on Zr atoms, while the top of the valence bands is predominantly on O atoms. This indicates that charge transfer during the delithiation may involve a significant charge change on O atoms, and this will be discussed further in the next section. The oxidation product of O^{2-} can be O^- or O_2, depending on the amount of charge transferred in the delithiation reaction.

The calculated orbital-energy band gap of Y-doped material calculated by PBE is about 3.0 eV, which is smaller than the calculated orbital-energy band gap of the pure LZO with the same functional, 4.9 eV. Similarly, the HSE06 calculations yielded a smaller gap (4.4 eV) compared to the undoped material (Figure 5a). In order to see the origin of the states contributing to the smaller gap more clearly, the partial charge density of the lowest unoccupied orbital at the Γ point is shown in Figure 5b. It is mainly located at the O vacancy site.

Table 2. Band Gap of Li_8ZrO_6 As Calculated Using Various Methods

	PW91	PBE	N12	M06-L	N12-SX	HSE	PBE0	PBE+U
band gap of Li_8ZrO_6	4.7[a]	4.9	5.0	5.3	6.5	6.8	7.5	5.1
mean |error|[b]	1.1	1.0	1.0	0.7	0.3	0.3		

[a]Ref 35. [b]For 31 semiconductors in ref 65.

DOI: 10.1021/jacs.5b04690
J. Am. Chem. Soc. 2015, 137, 10992−11003

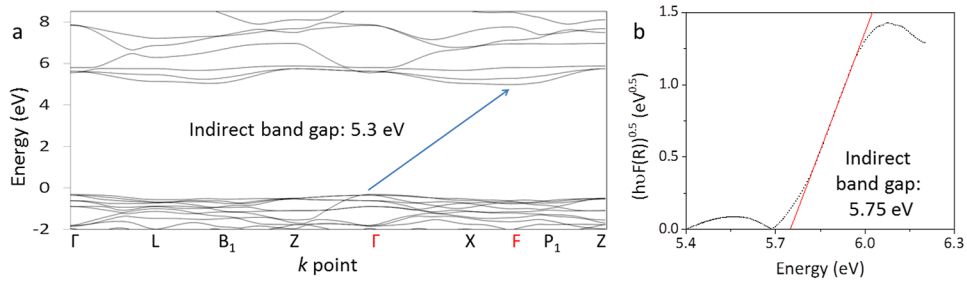

Figure 3. (a) Band structure of LZO calculated using M06-L, showing an indirect band gap of 5.3 eV. (b) The optical band gap of LZO was determined to be 5.75 eV using the Tauc plot obtained from a UV−vis spectrum.

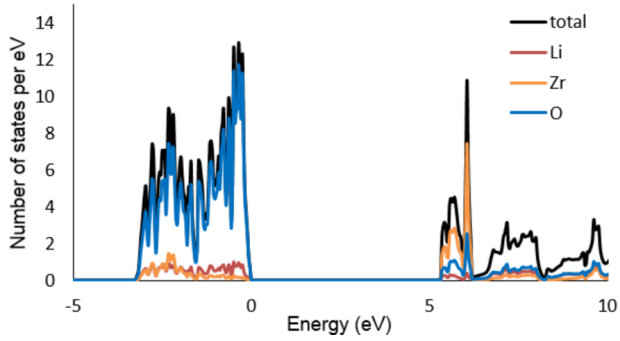

Figure 4. DOS and partial DOS of LZO using the M06-L functional.

3.3. Structures and Energies of Delithiated Li_xZrO_6. To understand the charging and discharging process at the atomic scale, we generated delithiated Li_xZrO_6 structures from the Li_8ZrO_6 structure. Table 3 shows the optimized volumes for the lowest-energy delithiated configurations of Li_xZrO_6 with x = 7, 6, and 5; more detailed information about the relative energies of various configurations is provided in Table S7. The frequencies of the lowest-energy configurations for the range of compositions from Li_8ZrO_6 to Li_5ZrO_6 were calculated, and no imaginary frequency was found at the Γ point. The M06-L, N12, PBE, PBE+U, and HSE06 functionals all predict the same most stable delithiation configurations.

In the cases of Li_7ZrO_6 and Li_6ZrO_6, we found that it is easier to remove Li atoms from tetrahedral interstitial sites than to remove them from octahedral sites. The volume of the unit cell and the structure both change very little when x is decreased to 7 and 6 in Li_xZrO_6; however, the distortion is very large when x is decreased to 5. The lowest-energy configuration is labeled Li5_x157 (where our notation is explained in Table 3), in which two tetrahedral Li atoms and one octahedral Li atom are removed, and the layered structure of the compound is destroyed. The smallest O−O distance becomes 1.34 Å in Li5_x157, and this is much shorter than the shortest distance, 2.96 Å, in LZO, and it is a typical distance for the superoxide O_2^-. The layered structure can be maintained in the case of Li5_x234 where three tetrahedral Li atoms are removed, but the volume is decreased by 10% compared with LZO, and this structure has an energy that is about 1 eV higher than that of Li5_x157. This indicates that two Li atoms may be topotactically removed without destroying the structures, while the extraction of the third Li atom may destroy the layered structure of LZO or greatly change the geometry.

For delithiated LZO, the M06-L, N12, and PBE functionals yield delocalized holes where the hole is delocalized over several oxygen atoms; these will be called itinerant holes. In contrast, PBE+U, HSE06, and N12-SX yield localized holes, which we will call small-polaron holes. The small-polaron holes are localized at one of the oxygen atoms close to the Li vacancy (see the magnetic moments of oxygen in Table S8). (The partial charge density for the lowest unoccupied orbital of $Li_{95}Zr_{12}O_{72}$ as calculated by the PBE and HSE06 functionals is shown in Figure S3.) Because the methods with screened exchange are known to give more accurate band structures than the local functionals,[45,49] we assume that the small-polaron hole is the correct prediction. Small-polaron holes are also found in Li_2O_2[67] and Li_2CO_3.[68]

In order to study the relative energies of the two possible hole structures, we attempted to optimize the structure with an itinerant hole by the HSE06 and PBE+U methods, but the HSE06 calculation failed, and the PBE+U calculation converged to a small-polaron structure. Therefore, we made an estimate by performing a single-point energy calculation on $Li_{95}Zr_{12}O_{72}$ with HSE06 at the structure optimized with PBE (details are in Table S9). This calculation gave an energy 0.8 eV higher than

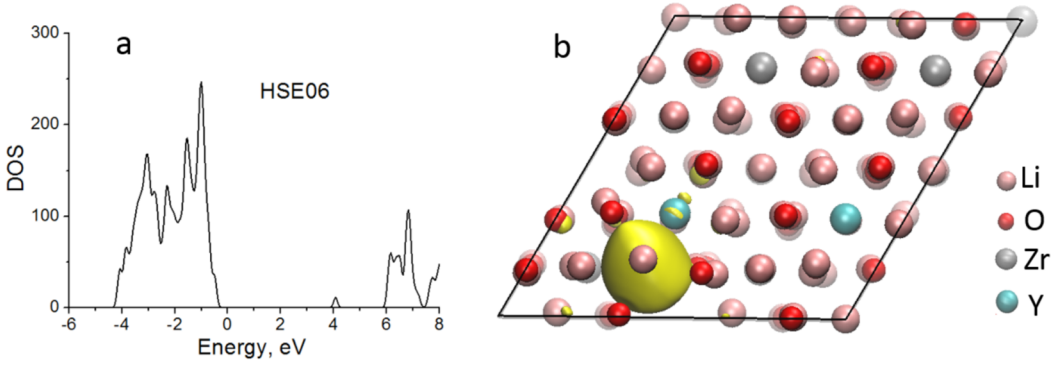

Figure 5. (a) DOS and (b) the partial charge density for the lowest unoccupied orbital for yttrium-doped LZO using the HSE06 functional.

DOI: 10.1021/jacs.5b04690
J. Am. Chem. Soc. 2015, 137, 10992−11003

Table 3. Volume (Å^3) per Formula Unit of the Lowest-Energy Li_xZrO_6 Configurations Found[a]

x	label[b]	PBE	N12	M06-L	HSE06
8	Li8	411	393	399	397
7	Li7_x1	408	393	396	399
6	Li6_x12	408	384	396	399
5	Li5_x157 (Li5_x234)[c]	426 (369)[c]	408 (348)[c]	414 (363)[c]	417 (369)

[a]These volumes refer to the conventional unit cells. [b]Li7_x1 means the delithiated configuration Li_7ZrO_6 is created by deleting the Li-1 as labeled in Figure 1b; Li6_x12 means the delithiated configuration Li_6ZrO_6 is created by deleting the Li-1 and Li-2; Li5_x157 means the delithiated configuration Li_5ZrO_6 is created by deleting the Li-1, Li-5, and Li-7 as labeled in Figure 1b; Li5_x234 means the delithiated configuration Li_5ZrO_6 is created by deleting the Li-2, Li-3, and Li-4. [c]Li5_x157 has much lower energy (~30 kcal/mol) than Li5_x234 (shown in Table S7), but the layered structure is not maintained, and an O−O bond is formed. Li5_234 is the most stable layered structure and is shown in parentheses.

the optimum HSE06 calculation with a localized hole. A similar calculation with PBE+U (also in Table S9) gave the same ordering, but a difference of only 0.5 eV. In the following, only the results for small-polaron holes are considered except where specified otherwise. The magnetic moment of the oxygen O9, where the hole is localized, is 0.68 μ_B with HSE06 and 0.70 μ_B with PBE+U, and the magnetic moments of other oxygens are <0.04 μ_B, which is negligible. The distances of the five nearest Li to the oxygen O9 are compared using different functionals (details are in Table S10 and Figure S4). The distances with HSE06 are close to the ones obtained with PBE+U but longer than the ones with PBE. The biggest difference is 0.42 Å. Since the O9 is oxidized in the localized-hole structure, it is less attracted to Li than is O^{2-} in the delocalized hole structure.

When two Li atoms are removed from $Li_{96}Zr_{12}O_{72}$, two small-polaron holes become localized on two different O atoms near the vacancies. For the lowest-energy configuration in which two Li vacancies are in adjacent tetrahedral layers, the O−O distance is 3.45 Å. The magnetic moment of the two oxygen atoms (O9 and O18) is 0.70 μ_B with HSE06 and 0.71 μ_B with PBE+U. (The partial charge density of the two lowest unoccupied orbitals at the Γ point is shown in Figure S5.) Similarly, the distances of the four nearest Li to the two O are longer in the localized structure. We also studied the local environment around the vacancy and compared the Li−O distances near the vacancies before and after the removal of Li (Figure S6). When Li9 is removed from $Li_{96}Zr_{12}O_{72}$ to form $Li_{95}Zr_{12}O_{72}$, large changes occur in the Li91−O18 and Li21−O9 distances; the Li91−O18 distance is decreased from 2.41 to 2.11 Å, and the Li21−O9 distance is increased from 2.12 to 2.47 Å. When Li18 is also removed, the Li−O distances change even more. The volume of the cell with the small-polaron hole is slightly bigger than that of LZO (details are in Table S11).

One Li vacancy leaves one hole in the valence band, which is mostly derived from O 2p states. The electronic structure calculations of the delithiated structures optimized by PBE and M06-L functional showed that the delithiated structures with itinerant holes are half-metals that are metallic in the minority-spin subband (details of the bands are in Figure S7). Small-polaron holes are predicted by the calculations with PBE+U, HSE06, and N12-SX. The DOS diagrams for $Li_{95}Zr_{12}O_{72}$ and $Li_{94}Zr_{12}O_{72}$ obtained by HSE06 are shown in Figure 6. An oxygen hole state can be observed just above the Fermi level for each Li removal. The calculated band gaps for the minority-spin subbands of $Li_{95}Zr_{12}O_{72}$ and $Li_{94}Zr_{12}O_{72}$ with HSE06 are 1.61 and 1.74 eV, respectively. The optical band gap of delithiated LZO should be smaller than this since the HSE06 orbital band gap overestimates the optical band gap of LZO. The band gap in the minority-spin subband increases as more Li are removed (Table 4). The hole prefers to localize on one of the oxygen

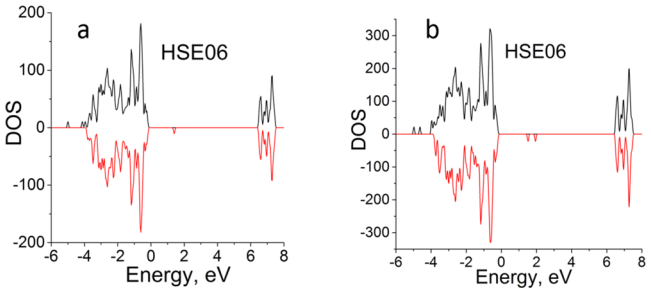

Figure 6. Calculated DOS of (a) $Li_{95}Zr_{12}O_{72}$ and (b) $Li_{94}Zr_{12}O_{72}$ using the HSE06 functional. The black curves are for the majority spin; by convention, this is the α spin (spin up). The red curves are for the minority spin; by convention, this is the β spin (spin down).

Table 4. Average Voltage Calculated Using HSE06 for the Topotactic Delithiation Path: $Li_8ZrO_6 \rightarrow (8-y)Li + Li_yZrO_6$, and the Calculated Gap of the Minority-Spin Subband of Li_yZrO_6

y	7.92	7.83	7.67	7.50	7.33	7.00	6.00
voltage (V)	4.09	4.06	4.18	4.12	4.02	4.04	3.93
spin-down gap (eV)	1.61	1.74	1.48	1.69	1.87	2.05	2.20

atoms next to the Li vacancy. These results clearly indicate that small-polaron holes tend to form near the Li vacancy. The removal of Li oxidizes O^{2-} to O^-.

Consistent with computational predictions (details are in Tables S7 and S11), the experiments showed very little change in structural dimensions after partial delithiation of Li_8ZrO_6 to approximately $Li_{7.62}ZrO_6$ (based on the measured discharge capacity) and subsequent relithiation, as shown in the PXRD patterns obtained for Li_8ZrO_6/C composite electrodes (Figure 7). Focusing on the characteristic (003), (101), and (012) peaks, no significant shift is observed during electrochemical cycling, confirming that the structure is maintained. The region of the XRD pattern in which reflections from a ZrO_2 phase would be observed does not show any evidence of crystalline ZrO_2 (the data are shown in Figure S8); this indicates that ZrO_2 is not formed during cycling, which in turn indicates a topotactic delithiation reaction.

From the lowest-energy configurations, we calculated the reaction energy for

$$Li_xZrO_6(s) \rightarrow Li_{x-1}ZrO_6(s) + Li(s) \quad (x = 8, 7, 6) \qquad (7)$$

and the results are shown in Table 5. The average voltages of the electrochemical cell derived by eq 6 are also shown in Table 5 for integer x. Although M06-L and HSE06 yield qualitatively different pictures of the delithiated structures, as already discussed, they predict the same voltages of 4.0 and 3.8 eV vs

DOI: 10.1021/jacs.5b04690
J. Am. Chem. Soc. 2015, 137, 10992−11003

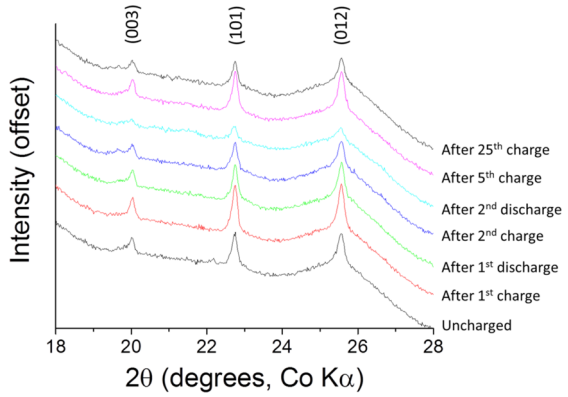

Figure 7. Partial ex situ PXRD patterns of electrode films made from a Li_8ZrO_6/C composite before charging and after the charge and discharge cycles indicated.

Table 5. Reaction Energy (kcal/mol) for $Li_xZrO_6(s) \rightarrow Li_{x-1}ZrO_6(s) + Li(s)$[a]

x	PBE	N12	M06-L	HSE06	PBE+U
8	85.0 (3.7)	84.4 (3.7)	92.5 (4.0)	92.9 (4.0)	71.1 (3.1)
7	82.2 (3.6)	79.3 (3.4)	87.0 (3.8)	88.1 (3.8)	66.9 (2.9)
6	53.7 (2.3)	54.9 (2.4)	58.8 (2.6)	56.8 (2.5)	70.8 (3.1)

[a]A positive energy corresponds to an endoergic reaction. The lowest-energy states from Table 3 are used. The numbers in parentheses are the corresponding average voltages (V) of the cell vs Li/Li^+.

Li/Li^+ for the extraction of the first and second lithium atoms, respectively. PBE+U generates similar geometric structures as HSE06, but it underestimates the voltage compared to HSE06 and experiment (Figure 8).

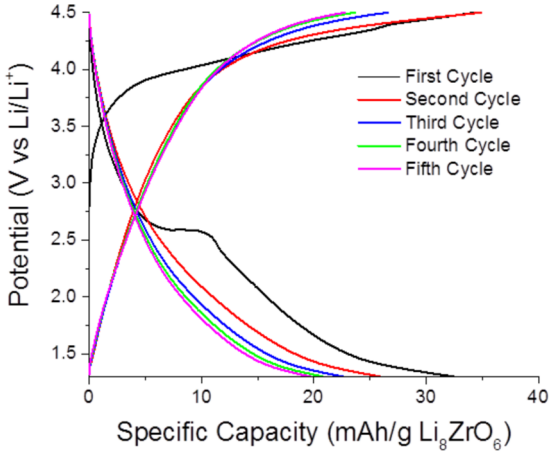

Figure 8. Galvanostatic charge/discharge curves of the coin cell used for the ex situ PXRD analysis. A current density corresponding to C/5 (per gram composite material) was used. This corresponds to 0.57C per gram LZO.

The second and third lithium atoms are easier to remove from the Li_8ZrO_6 structure than is the first lithium atom, indicating that the oxygen hole polaron is energetically more favorable at high lithium vacancy concentrations. This is similar to the result found previously for Li_2MnO_3.[69] Table 6 shows the results of a different delithiation path, in which the LZO is completely decomposed into $ZrO_2(s)$, Li(s), and $O_2(g)$. The voltage for this path is significantly lower than that of reaction 7; therefore, this decomposition path is more thermodynamically favorable. This indicates that the topotactic reaction path does not involve the most stable structures. Kang et al.[70] have studied the voltage profile for the delithiation of Li_2O_2 and compared two paths: one being the delithiation path from Li_2O_2 to xLi and $Li_{2-x}O_2$ and the other being decomposition of Li_2O_2 into 2Li and O_2. They found that the latter does not correspond to topotactic delithiation, and the first path may be kinetically more favorable, although the thermodynamic energy of reaction is less favorable. Similarly, we can compare the relative energy of the topotactic delithiation path and the equilibrium path for LZO by considering:

Table 6. Reaction Energy (kcal/mol) for $1/8Li_8ZrO_6(s) \rightarrow 1/8ZrO_2(s) + Li(s) + 1/4O_2(g)$[a]

PBE	N12	M06-L	HSE06
66.6 (2.9)	63.5 (2.8)	67.3 (2.9)	69.2 (3.0)

[a]The numbers in parentheses are the corresponding voltages (V) of the cell vs Li/Li^+.

$$\Delta E = E_{Li_xZrO_6} - \frac{x}{8}E_{Li_8ZrO_6} - \left(1 - \frac{x}{8}\right)E_{ZrO_2} - \left(2 - \frac{x}{4}\right)E_{O_2} \quad (8)$$

Assuming that the entropies of the solid phases and the pressure−volume contributions to the free energy are negligible, we consider only oxygen gas and the phonon free energy in calculating the difference between free energy and the energy (details are in Tables S12 and S13). This approximation has been successfully applied for the Li−Fe−P−O phase diagram.[71]

There are multiple off-stoichiometric Li_xZrO_6 configurations having relatively low energy above the equilibrium state, all of which have the Li vacancies at tetrahedral sites. The convex hull connecting the structures with the lowest relative energies is shown in Figure S9. The structures become more and more unstable as x decreases in Li_xZrO_6. The calculated voltages for the topotactic delithiation path $Li_8ZrO_6 \rightarrow (8 - y)Li + Li_yZrO_6$ are listed in Table 4. The predicted voltage for y = 7.0−7.92 is 4.02−4.18 V, consistent with the experimentally observed charging step at 4.3 V, indicating that these off-stoichiometric Li_yZrO_6 configurations are accessible in the charging process. The experimental galvanostatic charge curve for Li_8ZrO_6 at a charging/discharging rate of C/5 is given in Figure 8 and shows two very small step-like features in the range from 3.9 to 4.3 V during delithiation that may be associated with removal of the first and second lithium atoms in a part of the material. The first discharge cycle showed a step near 2.6 V, which could be the reformation of Li_8ZrO_6 from the Li_xZrO_6 formed during the delithiation. Because of the low conductivity of Li_8ZrO_6, the full sample (average grain size 108 nm) was likely not accessed during galvanostatic cycling, so that the observed capacity was still much below the theoretical value. Considering the high voltage requirements for delithiation and no ZrO_2 observed after cycling experimentally, we consider that the topotactic path in reaction 7 is kinetically favorable.

To increase the utilization of the cathode material, Y-doped ZrO_2 nanoparticles were employed as the LZO precursor, which together with the Super P carbon and the carbonization product from the lithium benzoate reduced the grain size to 51 nm at 900 °C calcination temperature and 31 nm at 700 °C calcination temperature. These grain sizes were estimated by applying the Scherrer equation to the full-width-at-half-

DOI: 10.1021/jacs.5b04690
J. Am. Chem. Soc. 2015, 137, 10992−11003

maximum of the (101) peak at 22.8°θ corrected for instrumental broadening (details are in Table S14). The smaller grain size, along with the additional carbon, was desirable to provide more intimate contact with the conductive carbon. These factors have been shown in other battery electrode materials to significantly improve electrochemical performance.[72−74] Besides influencing grain sizes, increases in the calcination temperature cause some changes to the elemental composition, most notably reducing the amount of a residual Li_2O impurity (see Table S14). On the basis of Raman spectra, the nature of the carbon matrix also changes with increasing calcination temperature, becoming more graphitic on the basis of a decreasing ratio in the relative intensity of the D- and G-bands observed in the Raman spectra (shown in Figure S10). The capacity of the materials in the first few cycles rapidly decreases (Figure 9) due to irreversible

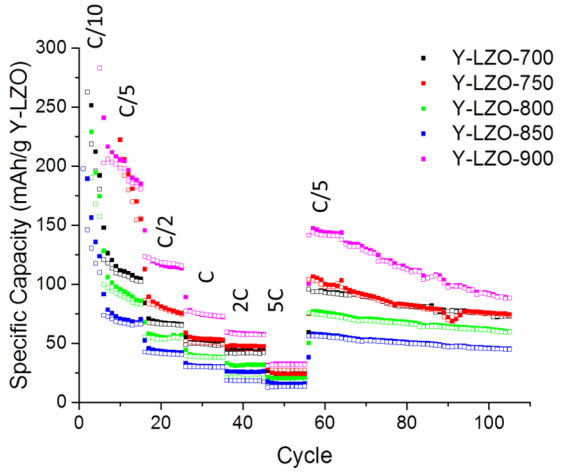

Figure 9. Specific capacity of the cell (per gram of Y-LZO) measured over more than100 cycles at the indicated C-rates, with the C-rate calculated per gram composite. The corresponding rates per gram of Y-LZO are 0.27, 0.53, 1.3, 2.7, 5.3, 13, and 0.53 C, respectively.

electrochemical reactions, probably related to cell conditioning such as formation of a solid−electrolyte interphase (SEI). After these cycles, significant capacity remains, with Y-LZO-900 showing a reversible capacity of over 175 mAh/g at C/5. The other samples also show reversible capacity higher than that of the undoped Li_8ZrO_6 sample. Furthermore, all samples can be cycled at rates as high as 5 C, with Y-LZO-900 showing a capacity of over 30 mAh/g. After 100 total cycles, Y-LZO-900 maintains over 100 mAh/g at a cycling rate of C/5, corresponding to almost a full Li^+ per formula unit. Considering cycles 60−105, the specific capacities decrease with increasing grain size (Table S14, 31−48 nm) as the synthesis temperature is increased. We therefore see the following trend in specific capacities: Y-LZO-700 ~ Y-LZO-750 > Y-LZO-800 > Y-LZO-850. All of these samples contain similar amounts of Li_2O as an impurity phase (Table S14). However, for the sample heated at the highest temperature (Y-LZO-900), much of this Li_2O phase is lost, and the estimated average grain size (51 nm) is similar to that of Y-LZO-850 (48 nm). With less inactive Li_2O, the fraction of active material is greater, hence the increase in specific capacity per gram of Y-LZO.

The first delithiation step for all of the Y-LZO samples showed the same general behavior as for the undoped samples, namely a rapid increase in the cell potential followed by a nearly asymptotical approach to the upper voltage limit. On the first discharge, a broad shoulder is observed that spans from 3.5 V to below 2.0 V as shown in Figure 10. After the first cycle, the

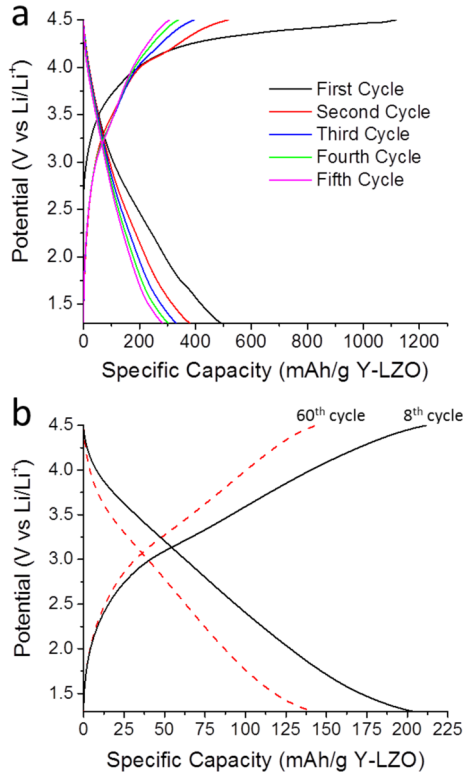

Figure 10. (a) Galvanostatic curves of the first five charge and discharge cycles for Y-LZO-900 carried out at C/10 (calculated per gram composite, 0.27 C per gram Y-LZO, see Figure 9). (b) Galvanostatic curves of the 8th and 60th cycle for Y-LZO-900, showing the shoulders relating to the lithiation and delithiation events. Both of these cycles were carried out at C/5 (calculated per gram composite, 0.53 C per gram Y-LZO), and the capacity is shown per gram Y−Li_8ZrO_6.

charging profile shows two inflection points, one at approximately 3.3 V and one above 4.0 V, corresponding to removal of the first and second Li^+ out of the material, while the discharge profile is unchanged. The calculated delithiation energies for $Li_{96}Zr_{10}Y_2O_{71} \rightarrow Li_{95}Zr_{10}Y_2O_{71} + Li$ and $Li_{95}Zr_{10}Y_2O_{71} \rightarrow Li_{94}Zr_{10}Y_2O_{71} + Li$ are 4.05 and 4.16 eV, respectively, using the HSE06 functional and 3.49 and 4.11 eV, respectively, with N12-SX. This is consistent with the experimental result: the voltage increases as more Li is removed, but it is different from the trend shown in Table 5 for LZO. These features remain constant for all cycles tested indicating that the mechanism for delithiation and relithiation does not change as the material is cycled (cycles 8 and 60 are shown for Y-LZO-900 in Figure 10a,b, respectively, as representative for all yttrium-doped samples). This behavior, along with the high capacities observed, shows that Li_8ZrO_6 is a promising novel cathode material for further study.

The quantum mechanical calculations suggest the following explanation for the increase in voltage as more Li are removed from Y-LZO. The delithiation in LZO and Y-LZO is associated with the oxidation of O^{2-} to O^-. In LZO and Li_2MnO_3, the voltage decreases as more Li ions are deintercalated, which we

DOI: 10.1021/jacs.5b04690
J. Am. Chem. Soc. 2015, 137, 10992−11003

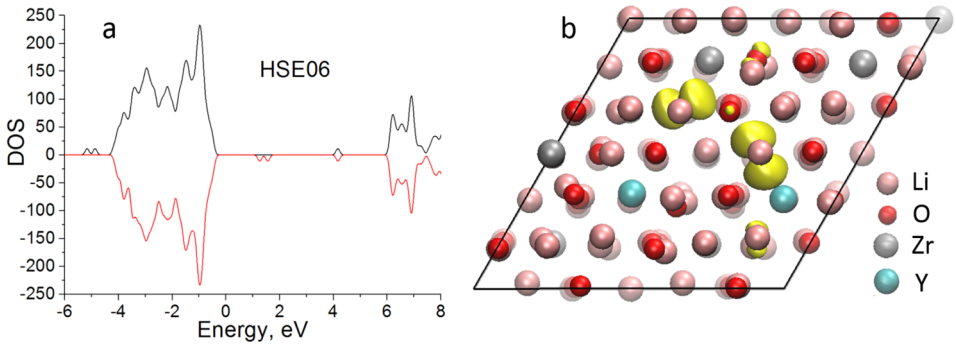

Figure 11. (a) The DOS of $Li_{94}Zr_{10}Y_2O_{71}$. The black curves are for the majority spin; by convention, this is the α spin (spin up). The red curves are for the minority spin; by convention, this is the β spin (spin down). (b) The charge density for the bipolaron of $Li_{94}Zr_{10}Y_2O_{71}$.

interpreted in the discussion of Table 5 as indicating that the oxygen hole polaron is energetically more favorable at high lithium vacancy concentrations. In Y-LZO, the substitution Y^{3+} for Zr^{4+} results in the creation of oxygen vacancies, so there is already a hole polaron at the oxygen vacancy before delithiation. Upon delithiation, there can be a repulsive interaction between the polaron at the void and the oxygen hole polaron, which results in the increase in voltage as more Li atoms are removed.

The DOS calculation with HSE06 shows that polaron hole states appear above the Fermi level for delithiated yttrium-doped LZO; they are located at the one of the oxygen atoms near the Li vacancy (Figure 11). The calculated band gaps for the spin-down electrons of $Li_{95}Zr_{10}Y_2O_{71}$ and $Li_{94}Zr_{10}Y_2O_{71}$ are 1.90 and 1.53 eV, respectively. The band gap of yttrium-doped LZO decreases as more Li are removed, which is different from the case for pure LZO. During the delithiation process, the magnetic moments of the Zr, Li, and Y atoms remain approximately zero, while the magnetic moments of one of the oxygen atoms near the Li vacancy are ~0.7 μB. This trend shows that the O atoms, rather than the Zr atoms, are being oxidized during the delithiation process. The partial oxidation of oxygen atoms was experimentally observed by XPS of a Li_8ZrO_6-containing cathode after charging of the cell by delithiation. The O 1s peak shifts from 530.3 eV in the uncharged (lithiated) electrode to a slightly higher binding energy of 530.6 eV after charging (partial delithiation to ca. $Li_{7.62}ZrO_6$) and then returns to 530.2 eV after discharge (Figure 12). The shift to higher binding energy can be associated with an increase in oxidation state of the oxygen as a result of the delithiation.[75,76] It should be noted that the oxygen peak contains an envelope of oxygen contributions from both Li_8ZrO_6 and oxygen atoms from the PF-derived carbon phase in the composite cathode, so that the actual shift from partially delithiated Li_8ZrO_6 may in fact be slightly larger.

We found that the LZO and Y-LZO are similar to olivine phosphates in that they exhibit polaronic hopping rather than band transport. In particular, the charge carriers in the delithiation for LZO and Y-LZO are hole polarons. In LZO, the hole polaron is bound to a Li^+ vacancy. In the earliest stage of delithiation, the conduction is very poor because of the low concentration of Li vacancies. As the delithiation proceeds, the conductivity may increase. We determined by PBE+U calculations that the lowest-energy path for Li-ion diffusion in LZO has a barrier of 0.395 eV. In the Y-doped LZO, we found that this same Li-ion diffusion path has a barrier that is 0.072 eV lower than the lowest-energy path for undoped LZO, and preliminary work indicates that other paths may have lower

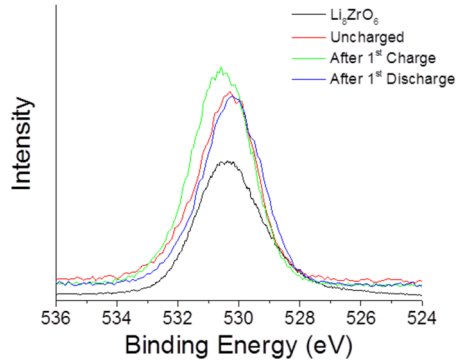

Figure 12. XPS spectra showing the position of the O_{1s} peak of a Li_8ZrO_6/C composite cathode before charging, after the first charge, and after the first discharge. A spectrum of neat Li_8ZrO_6 is included to demonstrate that the O_{1s} peak position is not affected by the composite preparation. The O_{1s} peak shifts to higher binding energy after partial delithiation, consistent with an increase in the oxidation state of oxygen.

barriers in the doped material. This indicates that Y-doping decreases the barrier for Li diffusion and should therefore increase the conductivity, in agreement with our original motivation for the doping. Furthermore, the higher surface-to-volume ratio and shorter diffusion distance in the smaller particles of Y-LZO also contribute to the improved conduction of the doped material.

3.4. Stability of Li_xZrO_6. We define the formation energy of Li_xZrO_6 as

$$\Delta E = \left(\frac{1}{8}\right)E_{Li_xZrO_6} - \left(\frac{x}{8}\right)E_{Li} - \left(\frac{1}{8}\right)E_{ZrO_2} - \left(\frac{1}{4}\right)E_{O_2} \quad (9)$$

We show the formation energy for the lowest-energy structure for each considered x in Figure 13. The formation energies of all structures in Figure 13 are negative, indicating that Li_xZrO_6 is stable. The formation becomes less exoergic as x decreases in Li_xZrO_6.

To test the stability of the delithiated compounds with respect to releasing oxygen, we extracted an oxygen atom from Li_xZrO_6 and calculated the reaction energy for $Li_xZrO_6(s) \rightarrow Li_xZrO_5(s) + 1/2O_2(g)$. The PBE, N12, and HSE06 results are given in Table 7. The three functionals give the same trends of the reaction energy. We found that when more lithium atoms are extracted from the crystal, it becomes easier to release oxygen in the form of O_2 gas. We found that for x = 8, 7, and 6.5, the reaction has a positive energy change, while the reaction has a negative energy change for x = 6. We conclude

DOI: 10.1021/jacs.5b04690
J. Am. Chem. Soc. 2015, 137, 10992−11003

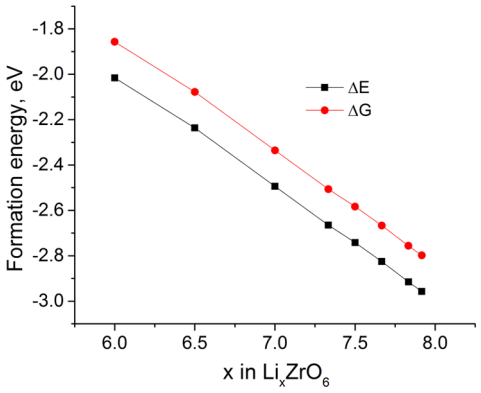

Figure 13. Formation energies for Li_xZrO_6 calculated with the HSE06 functional. At each x, multiple configurations are considered, and the formation energy of the lowest-energy configuration is given here.

Table 7. Reaction Energy (kcal/mol) for $Li_xZrO_6(s) \rightarrow Li_xZrO_5(s) + 1/2O_2(g)$.[a]

	O vacancy in		reaction energy		
x	Li_xZrO_6	Li_xZrO_5	PBE	N12	HSE06
8	Li8	10	153.5	151.0	161
7	Li7_x1	13	67.3	68.8	66.9
6.5			22.3		18.7
6	Li6_x12	10	−16.3	−17.5	−33.2
5	Li5_x157	11	6.8	3.9	6.2
5	Li5_x234	10	−28.5	−22.2	−33.3

[a]Calculated using PBE, N12, and HSE06. The numbers in the vacancy column correspond to numbers in Figure 1b. The lowest-energy configurations were used for calculations. A negative energy corresponds to an exoergic reaction. The oxygen atom that has the smallest Hirshfeld charge in Li_xZrO_6 was removed to form Li_xZrO_5. For x = 6.5, three Li atoms are removed from $Li_{16}Zr_2O_{12}$ cell, whereas for integer x, we used the primitive cell.

that in the charging and discharging process, Li_6ZrO_6 may be only metastable, and the charging is kinetically controlled. For x = 5, the layered structure can release O_2 exothermically, while the oxygen release reaction is endothermic for the distorted structure, which is more stable.

4. CONCLUSIONS

Theoretical and experimental studies on lithium-containing materials improve our understanding of Li-ion batteries. In the present study, we used Kohn−Sham density functional theory and a variety of experiments to study Li-ion battery cathodes, and we verified several predicted properties (band gap energy, structural and oxidation state changes during delithiation/relithiation, delithiation/relithiation potentials) experimentally. We have tested Li_8ZrO_6 as a new cathode material. We found that the Li_8ZrO_6 cathode has a large voltage of 4.0 eV vs Li/Li^+ for the delithiation of the first Li atom. The delithiation of Li_8ZrO_6 in a Li-ion battery is predicted to follow a nonthermodynamic path through the 4.0 V plateau with the oxygen atoms being oxidized. The structure is maintained with little volume change when one or two lithium atoms are extracted from Li_8ZrO_6, but the layered structure is greatly distorted when three lithium atoms are extracted. The delithiation product Li_6ZrO_6 is only metastable and may release O_2. Even if delithiation is limited to only two lithium atoms per formula unit, this material would have a theoretical capacity of 220 mAh/g, surpassing those of the current mainstream cathode materials $LiCoO_2$, $LiNiO_2$, $LiFePO_4$, and $LiMn_2O_4$. To achieve this capacity, it is necessary to overcome the low conductivity of Li_8ZrO_6. In electrode materials with similarly low conductivity ($LiFePO_4$, TiO_2), this has been achieved by nanostructuring, aliovalent doping, and forming intimate mixtures with conductive phases.[74] By doping the Li_8ZrO_6 with yttrium to reduce grain size and embedding the active material in a conductive carbon phase, it was indeed possible to achieve an initial specific capacity that nearly matched the theoretical capacity. Both HSE06 and PBE+U calculations show that Li removal creates a small-polaron hole on an oxygen near the Li vacancy for both LZO and yttrium-doped LZO. A challenge for future work is to achieve greater utilization of the Li-ion capacity and reduce the capacity fading in Li_8ZrO_6 as an active material for Li-ion battery cathodes.

5. EXPERIMENTAL AND COMPUTATIONAL DETAILS

5.1. Materials. Lithium nitrate (99%), zirconium oxynitrate hydrate (99%), yttrium nitrate hexahydrate (99%), lithium benzoate (98%), zirconium acetate hydroxide $[Zr(C_2H_3O_2)_x(OH)_y, x + y \approx 4]$, phenol (>99%), formaldehyde (aqueous solution, 37 wt %), tetrahydrofuran (THF, HPLC grade), *N*-methyl pyrrolidone (NMP, anhydrous, 99.5%), sodium hydroxide, and hydrochloric acid (∼37 wt %) were purchased from Sigma-Aldrich. Lithium acetate dihydrate was purchased from Johnson Matthey Company. Concentrated nitric acid was purchased from Macron Chemicals. Super P carbon, electrolyte (1 M $LiPF_6$ in 1:1:1 EC-DMC-DEC by volume), and PVDF were purchased from MTI Corporation. Carbon-coated aluminum foil was obtained from ExoPack. Celgard 3501 polypropylene membrane films were obtained from Celgard. Nitrate precursors were dried in an oven at 110 °C for at least 4 h prior to use to obtain a consistent mass. Deionized water was produced on site using a Barnstead Sybron purification system (final resistivity >18 MΩ·cm).

5.2. Preparation of Phenol-Formaldehyde Resol. A phenol-formaldehyde resol (PF) was prepared according to an established synthesis.[77] Briefly, phenol (61 g) was melted at 50 °C in a 500 mL glass round-bottom flask, and a 20 wt % aqueous NaOH solution (13.6 g) was then added dropwise. Aqueous formaldehyde (37 wt %, 200 mL) was subsequently added dropwise while stirring at 300 rpm with a Teflon-coated magnetic stir bar. The resulting solution was heated to 70 °C and left stirring for 1 h to increase the extent of polymerization. The as-made product was neutralized to pH ∼ 7 using aqueous HCl (0.6 M, ∼ 30 mL), followed by the removal of water through rotary evaporation. The polymer was redissolved in THF to a final concentration of 50 wt % and left to rest overnight to allow the precipitated NaCl to sediment. The polymer solution was decanted to obtain the final product and stored in a refrigerator as a stock solution until use.

The electrochemical tests were performed on an Arbin Instruments BT-2000 electrochemical interface.

5.3. Product Characterization. PXRD of the microcrystalline Li_8ZrO_6 powder was performed on a PANalytical X'Pert PRO diffractometer using a Co anode at 45 kV and 40 mA and an X'Celerator detector. Rietveld refinement was performed using PANalytical X'Pert Hi-Score Plus software to a final *R*-value of 4.39 and a goodness-of-fit of 10.1. Ex situ PXRD analysis was performed on composite electrodes by attaching the discs to an oriented Si wafer using Kapton tape to maintain a uniform sample height for all samples.

XPS was performed using a Surface Science SSX-100 spectrometer equipped with an Al anode operated at 10 kV potential and 20 mA current over a spot size of 0.64 mm^2.

Elemental analysis was performed using a Thermo Scientific iCAP 6500 dual view inductively coupled plasma optical emission spectrometer, operated at 1200 W with a nebulizer flow of 0.7 L/min, cooling gas at 12 L/min, and auxiliary gas at 0.5 L/min. An integration time of 8 s was used for each measurement, and five replicate measurements were carried out per sample. UV−vis spectra

DOI: 10.1021/jacs.5b04690
J. Am. Chem. Soc. 2015, 137, 10992−11003

were collected with a Thermo Scientific Evolution 220 spectrometer. Data were collected in the 190−800 nm range.

5.4. Density Functional Calculations. The quantum mechanical calculations were carried out using a locally modified version of the plane-wave-basis electronic structure program VASP.[78,79] The plane wave energy cutoff was set at 650 eV, and 6 × 6 × 6 Monkhorst−Pack *k*-point mesh was used for the calculations of primitive cell, except that the *k*-point grid was reduced to only the Γ point in the HSE06 calculations based on a 2 × 2 × 1 repetition of the conventional cell $Li_{24}Zr_3O_{18}$. The U correction was not applied to d orbitals. Projector-augmented-wave potentials[80,81] were used in all calculations. The energy criterion for self-consistency was set to <0.0001 eV/unit cell. The force convergence criterion for structure relaxation was set to <0.001 eV $Å^{-1}$. The XRD pattern was simulated using *Powdercell*.[82]

5.5. Free Energy Calculations. The phonon contributions to the free energy were calculated in the quasiharmonic approximation with the PHON program.[83] The entropy of O_2 gas was taken from experiment under standard conditions (298 K, 1 atm) and is 2.13 meV/K.[84]

■ ASSOCIATED CONTENT

Supporting Information

The Supporting Information is available free of charge on the ACS Publications website at DOI: 10.1021/jacs.5b04690.

Tables and figures showing structural data, PDOS, relative energies of delithiation, the convex hull, free energy calculations, elemental analyses and Raman data (PDF)

■ AUTHOR INFORMATION

Corresponding Authors

*a-stein@umn.edu

*truhlar@umn.edu

Author Contributions

§These authors contributed equally.

Notes

The authors declare no competing financial interest.

■ ACKNOWLEDGMENTS

The authors thank Anh Vu, Nam Tran, and William Smyrl for helpful discussions and collaboration on other aspects of the project, William Smyrl for access to his dry room and electrochemical equipment, and Lee Penn for use of her X-ray diffractometer. This material is based upon work that was supported by the U.S. Department of Energy, Office of Basic Energy Sciences, under award no. DE-SC0008662. Parts of this work were carried out in the University of Minnesota Characterization Facility, which receives partial support from the NSF through the MRSEC, ERC, MRI, and NNIN programs. This work was performed in part by using the Molecular Science Computing Facility in the William R. Wiley Environmental Molecular Sciences Laboratory of Pacific Northwest National Laboratory sponsored by the U.S. Department of Energy.

■ REFERENCES

(1) *Lithium Ion Batteries: Fundamentals and Performance*; Wakihara, M., Yamamoto, O., Eds.; Kodansha and Wiley: Tokyo and New York, 1998.

(2) Huggins, R. A. *Advanced Batteries: Materials Science Aspects*; Springer: New York, 2009.

(3) Goodenough, J. B.; Kim, Y. *Chem. Mater.* **2010**, *22*, 587−603.

(4) Etacheri, V.; Marom, R.; Elazari, R.; Salitra, G.; Aurbach, D. *Energy Environ. Sci.* **2011**, *4*, 3243−3262.

(5) *Lithium-Ion Batteries: Advanced Materials and Technologies*; Yuan, X., Liu, H., Zhang, J., Eds.; CRC Press: Boca Raton, FL, 2011.

(6) Zheng, J. M.; Xiao, J.; Yu, X. Q.; Kovarik, L.; Gu, M.; Omenya, F.; Chen, X. L.; Yang, X. Q.; Liu, J.; Graff, G. L.; Whittingham, M. S.; Zhang, J. G. *Phys. Chem. Chem. Phys.* **2012**, *14*, 13515−13521.

(7) Manthiram, A.; Murugan, A. V.; Sarkar, A.; Muraliganth, T. *Energy Environ. Sci.* **2008**, *1*, 621−638.

(8) Vu, A.; Qian, Y. Q.; Stein, A. *Adv. Energy Mater.* **2012**, *2*, 1056−1085.

(9) Cho, Y. J.; Kim, C. H.; Im, H. S.; Myung, Y.; Kim, H. S.; Back, S. H.; Lim, Y. R.; Jung, C. S.; Jang, D. M.; Park, J.; Lim, S. H.; Cha, E. H.; Bae, K. Y.; Song, M. S.; Cho, W. I. *Phys. Chem. Chem. Phys.* **2013**, *15*, 11691−11695.

(10) Fisher, C. A. J.; Islam, M. S. *J. Mater. Chem.* **2008**, *18*, 1209−1215.

(11) Kuganathan, N.; Islam, M. S. *Chem. Mater.* **2009**, *21*, 5196−5202.

(12) Adams, S.; Rao, R. P. *J. Mater. Chem.* **2012**, *22*, 1426−1434.

(13) Meng, Y. S.; Arroyo-de Dompablo, M. E. *Energy Environ. Sci.* **2009**, *2*, 589−609.

(14) Ceder, G. *MRS Bull.* **2010**, *35*, 693−701.

(15) Ceder, G.; Hautier, G.; Jain, A.; Ong, S. P. *MRS Bull.* **2011**, *36*, 185−191.

(16) Tang, Q.; Zhou, Z.; Shen, P. *J. Am. Chem. Soc.* **2012**, *134*, 16909−16916.

(17) Li, Y.; Wu, D.; Zhou, Z.; Cabrera, C. R.; Chen, Z. *J. Phys. Chem. Lett.* **2012**, *3*, 2221−2227.

(18) Jing, Y.; Zhou, Z.; Cabrera, C. R.; Chen, Z. *J. Phys. Chem. C* **2013**, *117*, 25409−25413.

(19) Bao, J.; Wu, D.; Tang, Q.; Ma, Z.; Zhou, Z. *Phys. Chem. Chem. Phys.* **2014**, *16*, 16145−16149.

(20) Van der Ven, A.; Aydinol, M. K.; Ceder, G.; Kresse, G.; Hafner, J. *Phys. Rev. B: Condens. Matter Mater. Phys.* **1998**, *58*, 2975−2987.

(21) Ceder, G.; Van der Ven, A. *Electrochim. Acta* **1999**, *45*, 131−150.

(22) Van der Ven, A.; Ceder, G. *J. Power Sources* **2001**, *97*−*98*, 529−531.

(23) Carlier, D.; Van der Ven, A.; Delmas, C.; Ceder, G. *Chem. Mater.* **2003**, *15*, 2651−2660.

(24) Bhattacharya, J.; Van der Ven, A. *Phys. Rev. B: Condens. Matter Mater. Phys.* **2010**, *81*, 104304.

(25) Van der Ven, A.; Marianetti, C.; Morgan, D.; Ceder, G. *Solid State Ionics* **2000**, *135*, 21−32.

(26) Van der Ven, A.; Thomas, J. C.; Xu, Q. C.; Swoboda, B.; Morgan, D. *Phys. Rev. B: Condens. Matter Mater. Phys.* **2008**, *78*, 104306.

(27) Yu, J. G.; Rosso, K. M.; Zhang, J. G.; Liu, J. *J. Mater. Chem.* **2011**, *21*, 12054−12058.

(28) Arroyo-DeDompablo, M. E.; Dominko, R.; Gallardo-Amores, J. M.; Dupont, L.; Mali, G.; Ehrenberg, H.; Jamnik, J.; Moran, E. *Chem. Mater.* **2008**, *20*, 5574−5584.

(29) Eames, C.; Armstrong, A. R.; Bruce, P. G.; Islam, M. S. *Chem. Mater.* **2012**, *24*, 2155−2161.

(30) Saracibar, A.; Van der Ven, A.; Arroyo-de Dompablo, M. E. *Chem. Mater.* **2012**, *24*, 495−503.

(31) Santamaria-Perez, D.; Amador, U.; Tortajada, J.; Dominko, R.; Arroyo-de Dompablo, M. E. *Inorg. Chem.* **2012**, *51*, 5779−5786.

(32) Longo, R. C.; Xiong, K.; Cho, K. *J. Electrochem. Soc.* **2013**, *160*, A60−A65.

(33) Kohn, W.; Sham, L. J. *Phys. Rev.* **1965**, *140*, A1133−A1138.

(34) Zou, Y.; Petric, A. *J. Phys. Chem. Solids* **1994**, *55*, 493−499.

(35) Duan, Y. *Phys. Chem. Chem. Phys.* **2013**, *15*, 9752−9760.

(36) Duan, Y. *J. Renewable Sustainable Energy* **2011**, *3*, 013102−013117.

(37) Neudecker, B. J.; Dudney, N. J.; Bates, J. B. Battery with an in-situ activation plated lithium anode. Patent WO2000060689 A1, October 20, 2000.

(38) Yin, X.-S.; Zhang, Q.-H.; Yu, J.-G. *Inorg. Chem.* **2011**, *50*, 2844−2850.

DOI: 10.1021/jacs.5b04690
J. Am. Chem. Soc. 2015, 137, 10992−11003

(39) Jiang, S.; Stangle, G. C.; Amarakoon, V. R. W.; Schulze, W. A. *J. Mater. Res.* **1996**, *11*, 2318−2324.
(40) Gopalan, R.; Chang, C.-H.; Lin, Y. S. *J. Mater. Sci.* **1995**, *30*, 3075.
(41) Kubelka, P.; Munk, F. *Z. Technol. Phys.* **1931**, *12*, 593−601.
(42) López, R.; Gómez, R. *J. Sol-Gel Sci. Technol.* **2012**, *61*, 1−7.
(43) Tauc, J.; Grigorovici, R.; Vancu, A. *Phys. Status Solidi B* **1966**, *15*, 627−637.
(44) Scholder, R.; Gläser, H. *Z. Anorg. Allg. Chem.* **1964**, *327*, 15−27.
(45) Krukau, A. V.; Vydrov, O. A.; Izmaylov, A. F.; Scuseria, G. E. *J. Chem. Phys.* **2006**, *125*, 224106.
(46) Zhao, Y.; Truhlar, D. G. *J. Chem. Phys.* **2006**, *125*, 194101.
(47) Peverati, R.; Truhlar, D. G. *J. Chem. Theory Comput.* **2012**, *8*, 2310−2319.
(48) Perdew, J. P.; Burke, K.; Ernzerhof, M. *Phys. Rev. Lett.* **1996**, *77*, 3865.
(49) Peverati, R.; Truhlar, D. G. *Phys. Chem. Chem. Phys.* **2012**, *14*, 16187−16191.
(50) Adamo, C.; Barone, V. *J. Chem. Phys.* **1999**, *110*, 6158−6170.
(51) Perdew, J. P. In *Electronic Structure of Solids '91*; Ziesche, P., Eschrig, H., Eds.; Akademie Verlag: Berlin, 1991; pp 11−20.
(52) Anisimov, V. I.; Aryasetiawan, F.; Liechtenstein, A. I. *J. Phys.: Condens. Matter* **1997**, *9*, 767.
(53) Dudarev, S. L.; Liechtenstein, A. I.; Castell, M. R.; Briggs, G. A. D.; Sutton, A. P. *Phys. Rev. B: Condens. Matter Mater. Phys.* **1997**, *56*, 4900.
(54) Mosey, N. J.; Liao, P.; Carter, E. A. *J. Chem. Phys.* **2008**, *129*, 014103.
(55) Nolan, M.; Watson, G. W. *Surf. Sci.* **2005**, *586*, 25−37.
(56) Nolan, M.; Watson, G. W. *J. Chem. Phys.* **2006**, *125*, 144701.
(57) Pardo, V.; Pickett, W. E. *Phys. Rev. B: Condens. Matter Mater. Phys.* **2008**, *78*, 134427.
(58) Adamo, C.; Barone, V. *J. Chem. Phys.* **1999**, *110*, 6158−6170.
(59) Mühle, C.; Dinnebier, R. E.; van Wüllen, L.; Schwering, G.; Jansen, M. *Inorg. Chem.* **2004**, *43*, 874−881.
(60) Delmas, C.; Maazaz, A.; Guillen, F.; Fouassier, C.; Réau, J. M.; Hagenmuller, P. *Mater. Res. Bull.* **1979**, *14*, 619−625.
(61) Bogicevic, A.; Wolverton, C.; Crosbie, G. M.; Stechel, E. B. *Phys. Rev. B: Condens. Matter Mater. Phys.* **2001**, *64*, 014106.
(62) Emeline, A.; Kataeva, G.; Litke, A.; Rudakova, A.; Ryabchuk, V.; Serpone, N. *Langmuir* **1998**, *14*, 5011−5022.
(63) Zhao, Y.; Truhlar, D. G. *J. Chem. Phys.* **2009**, *130*, 074103.
(64) Peverati, R.; Truhlar, D. G. *J. Chem. Phys.* **2012**, *136*, 134704.
(65) Peverati, R.; Truhlar, D. G. *Philos. Trans. R. Soc., A* **2014**, *372*, 20120476.
(66) Marenich, A. V.; Jerome, S. V.; Cramer, C. J.; Truhlar, D. G. *J. Chem. Theory Comput.* **2012**, *8*, 527−541.
(67) Ong, S. P.; Mo, Y.; Ceder, G. *Phys. Rev. B: Condens. Matter Mater. Phys.* **2012**, *85*, 081105(R).
(68) Garcia-Lastra, J. M.; Myrdal, J. S. G.; Christensen, R.; Thygesen, K. S.; Vegge, T. *J. Phys. Chem. C* **2013**, *117*, 5568−5577.
(69) Hoang, K. *Phys. Rev. Appl.* **2015**, *3*, 024013.
(70) Kang, S.; Mo, Y.; Ong, S. P.; Ceder, G. *Chem. Mater.* **2013**, *25*, 3328−3336.
(71) Ong, S. P.; Wang, L.; Kang, B.; Ceder, G. *Chem. Mater.* **2008**, *20*, 1798−1807.
(72) Petkovitch, N. D.; Rudisill, S. G.; Wilson, B. E.; Mukherjee, A.; Stein, A. *Inorg. Chem.* **2014**, *53*, 1100−1112.
(73) Vu, A.; Stein, A. *Chem. Mater.* **2011**, *23*, 3237−3245.
(74) Arico, A. S.; Bruce, P.; Scrosati, B.; Tarascon, J.-M.; van Schalkwijk, W. *Nat. Mater.* **2005**, *4*, 366−377.
(75) Dai, Y.; Manthiram, A.; Campion, A.; Goodenough, J. B. *Phys. Rev. B: Condens. Matter Mater. Phys.* **1988**, *38*, 5091−5094.
(76) Merino, N. A.; Barbero, B. P.; Eloy, P.; Cadús, L. E. *Appl. Surf. Sci.* **2006**, *253*, 1489−1493.
(77) Meng, Y.; Gu, D.; Zhang, F.; Shi, Y.; Yang, H.; Li, Z.; Yu, C.; Tu, B.; Zhao, D. *Angew. Chem., Int. Ed.* **2005**, *44*, 7053−7059.
(78) Kresse, G.; Furthmüller, J. *Comput. Mater. Sci.* **1996**, *6*, 15−50.
(79) Kresse, G.; Furthmüller, J. *Phys. Rev. B: Condens. Matter Mater. Phys.* **1996**, *54*, 11169−11186.
(80) Blochl, P. E. *Phys. Rev. B: Condens. Matter Mater. Phys.* **1994**, *50*, 17953−17978.
(81) Kresse, G.; Joubert, D. *Phys. Rev. B: Condens. Matter Mater. Phys.* **1999**, *59*, 1758−1775.
(82) Kraus, W.; Nolze, G. *J. Appl. Crystallogr.* **1996**, *29*, 301−303.
(83) Alfé, D. *Comput. Phys. Commun.* **2009**, *180*, 2622−2633.
(84) Chase, M. W., Jr.; Davies, C. A.; Downey, J. R., Jr.; Frurip, D. J.; McDonald, R. A.; Syverud, A. N. *NIST-JANAF Thermochemical Tables*; National Institute of Standards Technology: Gaithersburg, MD; http://kinetics.nist.gov/janaf/ (accessed May 5, 2015).

DOI: 10.1021/jacs.5b04690
J. Am. Chem. Soc. 2015, 137, 10992−11003